Pulsed Ion Microscope to Probe Quantum Gases

C. Veit,[1] N. Zuber,[1] O. A. Herrera-Sancho[1,2,3,4] V. S. V. Anasuri,[1] T. Schmid,[1] F. Meinert[1] R. Löw,[1] and T. Pfau[1,*]

[1]*5. Physikalisches Institut and Center for Integrated Quantum Science and Technology,*
Universität Stuttgart, Pfaffenwaldring 57, 70569 Stuttgart, Germany
[2]*Escuela de Física, Universidad de Costa Rica, 2060 San Pedro, San José, Costa Rica*
[3]*Centro de Investigación en Ciencia e Ingeniería de Materiales, Universidad de Costa Rica,*
2060 San Pedro, San José, Costa Rica
[4]*Centro de Investigación en Ciencias Atómicas, Nucleares y Moleculares, Universidad de Costa Rica,*
2060 San José, Costa Rica

The advent of the quantum gas microscope allowed for the *in situ* probing of ultracold gaseous matter on an unprecedented level of spatial resolution. However, the study of phenomena on ever smaller length scales, as well as the probing of three-dimensional systems, is fundamentally limited by the wavelength of the imaging light for all techniques based on linear optics. Here, we report on a high-resolution ion microscope as a versatile and powerful experimental tool to investigate quantum gases. The instrument clearly resolves atoms in an optical lattice with a spacing of 532 nm over a field of view of 50 sites and offers an extremely large depth of field on the order of at least 70 μm. With a simple model, we extract an upper limit for the achievable resolution of approximately 200 nm from our data. We demonstrate a pulsed operation mode enabling 3D imaging and allowing for the study of ionic impurities and Rydberg physics.

Subject Areas: Atomic and Molecular Physics

I. INTRODUCTION

The ability to observe natural phenomena on the single-particle level has led to major breakthroughs in modern physics. Prominent milestones in this context were the pioneering experiments in cloud chambers [1], the discovery of Rutherford scattering [2,3], the first imaging of a solid surface with atomic resolution [4], and the observation of quantum jumps for single trapped ions [5,6]. In the realm of quantum gases, time- and position-sensitive single-atom detection enabled Hanbury Brown-Twiss-type experiments for both bosons and fermions [7,8], and a scanning electron microscope was used for the first high-resolution *in situ* detection of individual atoms [9,10]. Nowadays, optical quantum gas microscopes offer the possibility to image strongly interacting atoms loaded into optical lattices with single-site resolution [11,12] and have been used to investigate Bose- and Fermi-Hubbard physics [13–16]. Image-stacking techniques have been employed for the reconstruction of three-dimensional atomic structures [17,18], and ensemble-averaged imaging with

superresolution has been demonstrated [19,20]. All microscopes based on linear optics, however, are fundamentally limited in their resolution and depth of field by the wavelength of the imaging light. A high-resolution imaging method capable of extracting three-dimensional information from large-volume bulk gases is therefore highly desirable and would allow for the study of quantum correlations, impurity physics, and transport phenomena in unprecedented ways.

Here, we present a high-resolution imaging system based on ion optics, offering a multitude of intriguing features. Charged-particle optics is commonly employed in cold-atom experiments in the form of momentum-space spectrometers [21,22], but it has also been used to image neutral ground-state atoms [9,23,24] and Rydberg atoms [24–28]. Our instrument is especially inspired by the ion microscope presented in Ref. [23], for which a spatial resolution of smaller than 2.7 μm was demonstrated, and it is based on the following simple concept (Fig. 1). Neutral atoms are converted into ions and are subsequently imaged by means of a magnification system onto a spatially and temporally resolving detector. This scheme allows for the investigation of ground-state ensembles, Rydberg excitations, and ionic impurities with the very same apparatus. Owing to the excellent time resolution of the instrument on the order of a few nanoseconds (see Appendix D), both time-dependent measurements and 3D imaging via the time-of-flight information can be realized [29]. The choice of the ionization process constitutes a powerful experimental tool,

*t.pfau@physik.uni-stuttgart.de
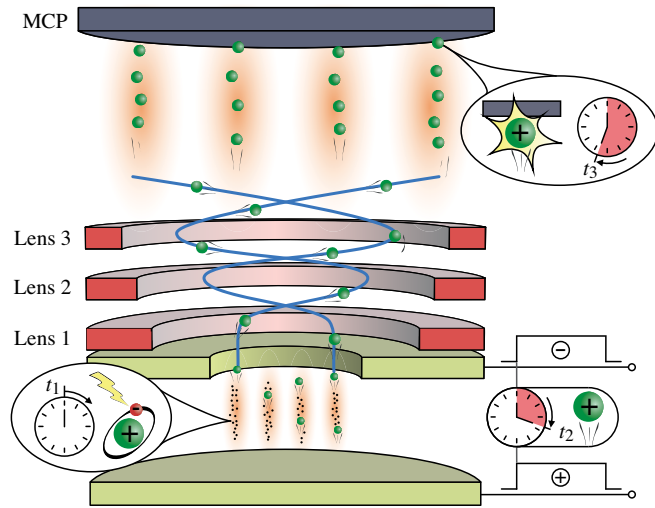
FIG. 1. Concept of the pulsed ion microscope. Neutral atoms in a quantum gas (shown in a 1D periodic potential) are converted into ions at time $t = t_1$ via a suitable ionization process (e.g., near-threshold photoionization). After a variable wait time, an extraction field is pulsed on ($t = t_2$), and the ions are imaged onto a spatially resolving detector by means of an ion microscope consisting of three electrostatic lenses ($t = t_3$). The high time resolution of the multichannel plate detector (MCP) allows for the study of dynamical processes (e.g., in strongly interacting many-body systems) and 3D imaging via the time-of-flight information. The versatile nature of the concept enables the study of ground-state ensembles, Rydberg systems, and ionic impurities.

FIG. 2. Ion microscope. The microscope column consists of three electrostatic lenses (main electrodes marked in red, drift sections in gray). Each lens is followed by an electrostatic quadrupole deflector (blue). (a) The object plane lies above a repeller electrode and below an extractor electrode (pale yellow), which, at the same time, are part of a six-plate electric field control (radial field plates marked in blue). The repeller hosts an indium-tin-oxide-coated aspheric optical lens. The extractor also acts as the lower lens electrode of the first lens. (b) Detailed view of the second lens and the following deflection stage. (c) Spatially resolved ion detection is achieved via a delay-line anode on top of an MCP stack. (d) Schematic representation of the electrode configuration. Imaging properties and magnification are determined by the extraction voltages (V_E and V_R), the lens voltages (V_1 to V_3), and the drift-tube voltages (V_{D1} and V_{D2}). The latter are referred to as V_D for all measurements for which $V_{D1} = V_{D2}$.

enabling the combination of the high spatial resolution with spectroscopic techniques and permitting weak measurement schemes. Furthermore, near-threshold photoionization offers the possibility to produce ultracold ions [30] and opens the door to the spatially resolved study of ionic impurities and ion-atom scattering in the quantum regime [31–35]. In this context, an exciting prospect is the observation of polaron formation and transport dynamics from the two-body collisional timescale to the few- and many-body timescales. We foresee further applications of our approach in the imaging of spatial ordering in three-dimensional Rydberg-blockaded ensembles [36], the detection of fine spatial structures in bulk Fermi gases (e.g., Friedel oscillations [37] and spatial correlations), and the probing of dynamic many-body processes with a high time resolution, just to name a few examples. In the following, we briefly describe our ion microscope and then focus on its performance and imaging characteristics. We begin by discussing a continuous operation mode, in which the object plane is permanently immersed in an extraction field, before demonstrating a pulsed extraction scheme especially suited for the study of ions and Rydberg atoms.

II. ION MICROSCOPE

The design of our ion microscope is depicted in Fig. 2. The whole microscope column has a length of 135 cm and

consists of three electrostatic three-cylinder lenses [38] connected via field-free drift sections. In order to compensate for mechanical tolerances, each lens is followed by a quadrupole deflector. The object plane lies between a repeller and an extractor electrode, the latter of which also acts as the lower lens electrode of the first lens. To allow for the study of Rydberg atoms [39] and ions in a field-free environment, the extraction field can be pulsed on a timescale of 30 ns. The observation of free ions serves as an excellent probe for stray electric fields, which we cancel by applying small compensation voltages to the extractor and repeller as well as to four radially arranged field plates (see Appendix I). A schematic of the electrode configuration is shown in Fig. 2(d). The ions are detected with an MCP in combination with a delay-line detector [40] offering a high spatial and temporal resolution on the order of 100 μm and 200 ps, respectively [41]. We expect the

detection efficiency of our MCP to be limited to a value close to the open-area ratio of about 70% [42] and plan to improve this efficiency in the future by employing a funnel-type MCP offering an open-area ratio of 90% [43]. As detailed in Appendix D, we aim for a further enhancement of the detection efficiency by exploiting facilitated Rydberg excitation around ionic seeds (see Ref. [44] and references within). More information on our instrument can be found in Ref. [29].

In contrast to most conventional optical systems, electrostatic lens systems offer easy tunability of imaging properties via the electrode voltages. We explore the parameter space of our ion microscope by means of numerical trajectory simulations performed with a commercially available program [45] and find that our system allows for both 2D and 3D imaging. In a first step, we focus here on the performance of our microscope regarding 2D imaging. Nevertheless, a first proof-of-principle experiment demonstrating the 3D imaging capabilities of the optics is presented at the end of this paper. In the 2D mode, we keep all drift tubes at the potential of the MCP front plate (-2.4 kV) and employ typical extraction voltages of $V_E = -V_R = -500$V, corresponding to an electric field of approximately 420 V/cm in the object plane. An example of the axial electrostatic potential is shown in Appendix A. Owing to their small initial velocity, the cold ions are extracted on trajectories almost parallel to the extraction field. Consequently, a sharp projection of the object plane can be observed in the detector plane even for voltage configurations for which no actual image formation occurs.

III. CHARACTERISTICS OF THE IMAGING SYSTEM

In the following, we present experimental results on the characteristics of the previously described imaging system. For most of the measurements, ^{87}Rb atoms were loaded into a one-dimensional optical lattice with a spacing of 532 nm and photoionized in the crossing volume of two laser beams with wavelengths of 780 nm and 479 nm. The 780-nm beam was blue-detuned by 78 MHz from the $|5P_{3/2}, F = 3\rangle$ intermediate state and aligned parallel to the optical axis of the microscope (z direction, see Fig. 2). The 479-nm beam was aligned perpendicular to the optical axis (y direction) and tuned such as to realize a near-threshold ionization with typical excess energies on the order of $h \times 100$ GHz or below, where h corresponds to the Planck constant. The setup described above was used to characterize the magnification, field of view (FOV), depth of field (DOF), and resolution of our microscope. The waists of the ionization beams were shaped to suit the specific measurement.

The study of the magnification behavior of the ion optics included magnifications too small to resolve the optical lattice. For the corresponding set of measurements, we held the atoms in an optical dipole trap and induced a spatial

structure of the 780-nm light field by projecting the diffraction pattern of a double slit onto the atoms. The period of the resulting ionization pattern was measured to be 6.9 μm by employing a large magnification and using the optical lattice as a ruler. A similar approach was utilized in the proof-of-principle experiment demonstrating 3D imaging, and it is detailed in the corresponding section.

For all characterization methods, the imaged ion distribution was determined by the atomic density distribution and the intensity profiles of the ionization beams. The presented measurements are integrated over several experimental cycles and, as detailed later, compensated for phase drifts of the optical lattice as well as for minor distortions of the detected images. Additional information on the experiment and the data evaluation is given in the appendix.

A. Magnification

To explore the exceptional tunability of the magnification M of our instrument, we fix all electrode voltages but V_2 and V_3 (see caption of Fig. 3) and use the latter two to tune the focal lengths of the second and third lens. Figure 3(a) shows a corresponding simulation of the total magnification revealing that high-quality imaging results can be obtained for magnifications ranging from below $\times 200$ to above $\times 1500$. Both higher and lower magnifications can be achieved if additional electrode voltages are adjusted. We compare the behavior of our microscope with the simulation for scans of either V_2 [Fig. 3(c)] or V_3 [Fig. 3(b)] for which the respective other voltage was fixed [see red lines in Fig. 3(a)]. As delineated above, the magnification was extracted by imaging either atoms in an optical lattice or a diffraction pattern of known period (see insets). Evidently, the simulations describe our imaging system accurately, with the largest deviation from the experiment being smaller than 10%. For our detector diameter (40 mm), the demonstrated magnification range maps to a FOV between approximately 30 μm and 300 μm, which permits both high-resolution studies and the observation of large atomic ensembles.

B. Field of view

In order to confirm that the large magnifications suitable for high-resolution imaging can be used without any sacrifices concerning the FOV, we utilized our optical lattice as a test pattern. To this end, we employed a large 780-nm beam ($w_{780} \approx 36$ μm) and shaped the 479-nm beam to a horizontal light sheet with a waist of $w_{x,479} \approx 40$ μm. The measurement shown in Fig. 4(a) illustrates that the lattice can be clearly resolved over the whole detector area, corresponding to a FOV of 50 lattice sites. The data shown are postprocessed in two ways (see also Appendix F). First, we make use of the regular structure of the lattice to compensate for a local phase Φ_l caused by small distortions common to all measurements [Fig. 4(d)]. Second, we compensate for a time-
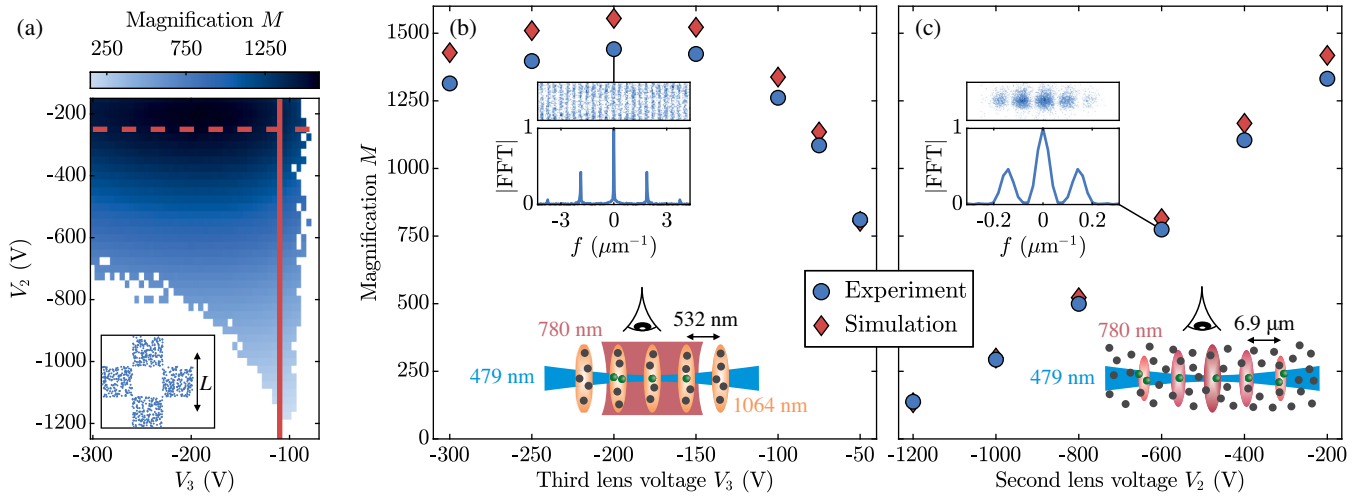
FIG. 3. Tuning of the magnification. A large range of M is achievable by tuning V_2 and V_3 ($V_E = -V_R = -500$ V, $V_1 = -3.2$ kV, $V_D = -2.4$ kV). (a) Result of numerical trajectory simulations for a test pattern with a line spacing of $L = 100$ nm (see inset) and parameters resembling the experimental situation. For the displayed data points, the line spacing is clearly resolved and low image distortion is present (see Appendix A for details). Most values of M are accessible by tuning only V_2. (b) Comparison between experiment and simulation along the dashed red line ($V_2 = -250$ V) shown in panel (a). The atoms were loaded into a retroreflected 1064-nm lattice and photoionized in a crossed-beam configuration ($w_{780} \approx 26$ μm, $w_{479} \approx 5$ μm). (c) Comparison between experiment and simulation along the solid red line ($V_3 = -110$ V) shown in panel (a). The 780-nm photoionization laser was spatially structured by projecting the diffraction pattern of a double slit onto the atoms (see Appendix E). As an example, the insets in panels (b) and (c) show a cutout of the postprocessed detector image along with the normalized magnitude of the fast Fourier transform (FFT) for one of the voltage configurations. The FFT corresponds to the integrated profile of the whole image in object coordinates. The values of M are inferred from the period of the detected patterns. All experimental error bars (see Appendix E) are significantly smaller than the marker size.
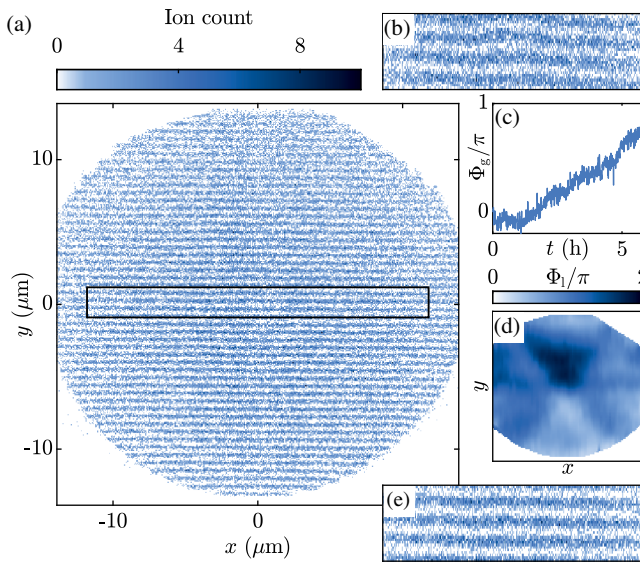
FIG. 4. Field of view. The FOV was investigated for the voltage configuration corresponding to the largest magnification shown in Fig. 3(b) ($M = 1441$). (a) Measured data (sum over 1200 experimental cycles, object coordinates), corrected for a global phase Φ_g (drift of the lattice) and a local phase Φ_l (distortion). The marked region is enlarged in panels (b) (raw data) and (e) (phase-corrected data). Panel (c) shows Φ_g over time, and panel (d) shows Φ_l as a function of the spatial coordinates. The local phase Φ_l is extracted from the local deviation of the experimental data from the expected regular lattice structure.

dependent global phase Φ_g caused by a thermal drift of the lattice over the measurement time of almost six hours [Fig. 4(c)]. We find that the local phase Φ_l stays below 2π over the whole detector, and we use the data shown in Fig. 4(d) to compensate for the observed distortion in all our measurements. A comparison between the raw data and the postprocessed data is shown in Figs. 4(b) and 4(e) for the marked region in Fig. 4(a). Even the raw data show a good contrast.

C. Depth of field

The FOV and DOF of an imaging system determine the maximum dimensions of the objects that can be imaged. In the case of high-resolution optical microscopes, the imaging volume is typically restricted by a small DOF originating from the large numerical aperture of the systems. In contrast, the DOF of our ion microscope is remarkably large, as demonstrated in the following. The DOF was probed for the same voltage configuration as used for the FOV measurement by employing a large 780-nm beam ($w_{780} \approx 36$ μm) and by shaping the 479-nm beam to a vertical light sheet ($w_{x,479} \approx 2$ μm, $w_{z,479} \approx 100$ μm). Because of the large extent of the light sheet in the z direction, the height of the ionization region was primarily limited by the diameter of the atomic cloud ($1/e$ diameter of approximately 70 μm). Careful alignment of the lattice planes was required in order to attain a good imaging
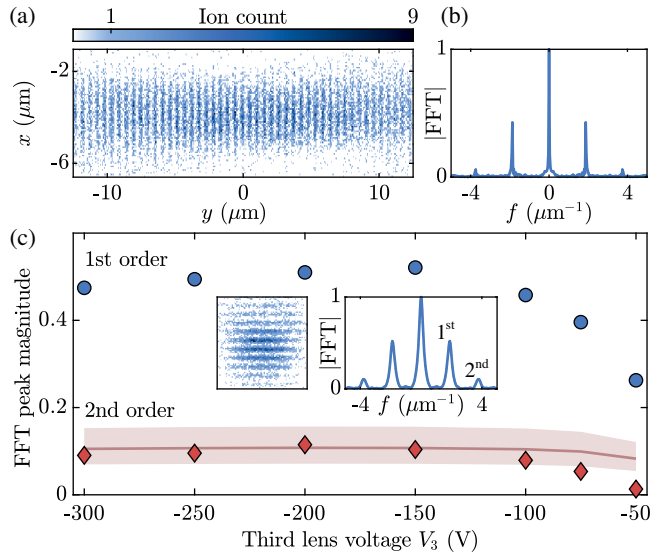
FIG. 5.   Depth of field and resolution. (a) Imaging result for an increased depth of field limited only by the cloud size ($1/e$ diameter of 70 μm). (b) Absolute value of the FFT corresponding to the integrated lattice profile shown in panel (a). (c) Magnitudes of the first- and second-order FFT peaks (here, as a function of V_3 and for a tightly confined ionization region) serving as a qualitative measure of the resolution. All experimental error bars (see Appendix F) are smaller than the marker size. The insets show the experimental data for $V_3 = -150$ V. The solid line and the shaded area show the theoretical prediction for the upper bound of the second-order peak amplitude for a resolution of 200 ± 20 nm. Experimental circumstances are detailed in the main text.

contrast. A resulting measurement is shown in Fig. 5(a), along with the normalized magnitude of the FFT corresponding to the integrated lattice profile [Fig. 5(b)]. As expected from simulations, we find that the imaging result does not suffer from the increased DOF and that it is very similar to the results obtained from the magnification measurements [see inset of Fig. 3(b) for comparison]. Given the diameter of the atomic cloud, we can quantify the DOF to be on the order of at least 70 μm. In comparison with quantum gas microscopes, typically featuring a DOF smaller than a few micrometers, the DOF of our ion optics is exceptionally large and allows for the study of three-dimensional bulk gases.

D. Resolution

From the measurements presented above, it is evident that, for large magnifications, the resolution of the microscope is significantly smaller than the period of our test target given by the optical lattice. In order to still characterize the resolution, we take advantage of the localization of the atoms caused by the tight confinement in the optical lattice. The signature of this localization is found in the FFT of our measured data, in which a signal at twice the lattice frequency is apparent [see, e.g., Fig. 5(b)]. We use the

amplitude of this second-order peak as a qualitative measure of the resolution R of our microscope, and we use a simple model to give a quantitative upper limit of R. Because of the finite detector resolution, we expect our imaging system to perform best at large magnifications. Consequently, the voltage configuration corresponding to the data shown in Fig. 3(b) was chosen for our resolution studies. In order to minimize the effects of residual distortions, a tightly confined photoionization volume was used for the measurement ($w_{780} \approx 2$ μm, $w_{479} \approx 5$ μm). Figure 5(c) shows the magnitude of the first- and second-order FFT peaks corresponding to the measured data as a function of V_3. The significant amplitude of the second-order peak indicates an excellent resolution over almost the whole measurement range. The drop of contrast at small magnitudes of V_3 is in accordance with our simulations and results from both imaging aberrations and a decrease of magnification.

To extract an upper limit of the resolution, we assume that all atoms occupy the lowest band of the optical lattice and employ a Gaussian approximation for the single-site wave function (see Appendix H for details). We then convolve the density profile with a Gaussian point spread function (PSF), scale it according to the magnification of the microscope, and bin the profile with the bin size used for the experimental data (100 μm). Expectedly, the FFT of the model profile shows a second-order peak at twice the lattice frequency, enabling comparison with the experiment. We identify the full width at half maximum of the PSF as the resolution R and find that, for the highest magnifications, we get good agreement with our experimental data for $R \approx 200$ nm [see solid line in Fig. 5(c)]. In consideration of the nonoptimized loading procedure of the optical lattice, the atoms most certainly occupy several bands instead of only the lowest band. Since this leads to a less-confined wave function (and therefore to a smaller amplitude of the second-order FFT peak), the actual resolution of our microscope is probably significantly smaller than 200 nm. Indeed, numerical simulations accounting for realistic mechanical tolerances and voltage noise suggest that a resolution on the order of 100 nm is achievable [29], which permits the *in situ* observation of phenomena taking place at the length scale of the healing length of Bose-Einstein condensates [46] or the Fermi wavelength of ultracold Fermi gases [37].

E. Pulsed operation

A powerful feature of our ion microscope is the ability to directly image ions and field-ionized Rydberg atoms. Both the study of Rydberg and ion physics, however, would be hindered by a constant extraction field. Therefore, our instrument is designed such as to allow for a pulsed extraction. In the measurements presented in the following, a fast high-voltage switch was employed to toggle between small compensation voltages and large extraction voltages
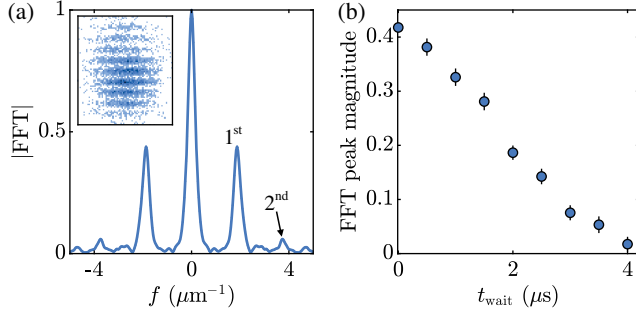
FIG. 6. Pulsed operation mode. (a) Imaging result for $t_{wait} = 0$ μs and magnitude of the FFT corresponding to the integrated lattice profile. The clear signature of a second-order Fourier peak indicates a resolution on the order of half the lattice spacing (266 nm). (b) Decay of the first-order FFT peak, which serves as an indicator for the blurring of the lattice structure as a function of t_{wait}. The timescale of the decay reveals the low temperature of the produced ions in the few tens of microkelvin range. Error bars correspond to a conservative estimate of the statistical error (see Appendix F).

being applied to the extractor and repeller [Fig. 2(a)]. By the additional use of four radial field plates, this procedure enables us to precisely cancel stray electric fields while the extraction field is switched off. The pulsed operation mode was tested for the same optical configuration as was used for the measurements discussed in the previous paragraph and slightly different voltage settings resulting in a magnification of $M = 1467$ (see Appendix G). In every experiment, 6000 ionization cycles were realized, each consisting of a 1-μs-long photoionization pulse followed by a variable wait time t_{wait}, after which the extraction field was switched on. A measurement result for $t_{wait} = 0$ μs is shown in the inset of Fig. 6(a), together with the corresponding FFT. As for the data measured in the continuous operation mode, second-order Fourier peaks are clearly observable and indicate a resolution on the order of half the lattice spacing. For increasing wait time t_{wait}, the visibility of the lattice structure decreases, and a decay of the first-order Fourier peak can be observed [Fig. 6(b)]. This approximately Gaussian-shaped decay with a $1/e$ timescale of 2.4 μs is consistent with an ion temperature of a few tens of microkelvin. We attribute the associated kinetic energy mostly to the excess ionization energy ($\sim k_B \times 13$ μK, with k_B being the Boltzmann constant) and the occupancy of several excited bands in the optical lattice. A reduction of the ionization energy in combination with an ultracold atomic sample will, in the future, allow for the creation of much colder ions and enable the investigation of ion-atom hybrid systems in the quantum regime.

F. 3D imaging

The 3D imaging capability of our instrument is based on the time-of-flight information of the ions. For the following discussion, it is worth recalling that the ions are created between two electrodes essentially resembling a plate capacitor [Fig. 2(a)]. Owing to the linear variation of the extraction potential along the z direction, the ions pass the extractor electrode with a kinetic energy depending on the initial position along the optical axis. As a consequence, the axial position directly maps to a small variation of the overall time of flight of the ions. Our simulations show that, for a broad range of operating conditions, the mapping between the object coordinate z and the time of flight t_{tof} is accurately described by the relationship

$$t_{tof}(z, r) = \alpha z + t_r(r) + t_0. \tag{1}$$

Here, α is a distance-to-time conversion factor, r is the initial radial distance from the optical axis, $t_r(r)$ describes a radially symmetric curvature of the time of flight, and t_0 is a position-independent offset. It should be emphasized that, for typical operating conditions, t_0 is on the order of tens of microseconds, whereas the contribution of the other two terms is in the nanosecond range. While t_r constitutes an unwanted distortion, the associated curvature only needs to be measured once and is then easily compensated for during postprocessing.

For a given time resolution (see Appendix D), the achievable axial resolution depends on α and increases with the overall time of flight of the ions. Consequently, it is beneficial to employ drift-tube voltages of small magnitude. While all drift tubes were kept at the potential of the MCP front plate (−2.4 kV) for the measurements presented in the preceding part of this paper, our microscope is specifically designed such as to allow for a tuning of V_{D1} [see Fig. 2(d)]. Figure 7(a) shows a simulation of the transverse magnification M of the microscope, demonstrating that a large range of M is also accessible for $V_{D1} = -550$ V. Details on the performed simulations can be found in Appendix A.

As a first test of the 3D imaging capabilities of the microscope, we performed a proof-of-principle experiment in which we resolved the diffraction pattern of two crossed double slits. For the chosen electrode voltage configuration [marked with a red dot in Fig. 7(a)], the transverse magnification was experimentally determined from an optical lattice measurement to be $M = 1026$, which is in good agreement with the simulated value of $M_{sim} = 1080$. The atomic cloud was prepared similarly to the procedure detailed in Appendix B, but it was transported and held in a single-beam 1064-nm optical dipole trap oriented along the x direction ($w_{1064} \approx 38$ μm). As for the pulsed measurements shown in Fig. 6, every ionization cycle consisted of an approximately 1-μs-long photoionization pulse, after which the extraction field was switched on. The complete ionization sequence lasted 1.3 s and comprised approximately 4300 ionization cycles. During the photoionization pulse, the central part of the atomic cloud was illuminated homogeneously by a large 780-nm beam. The 479-nm light
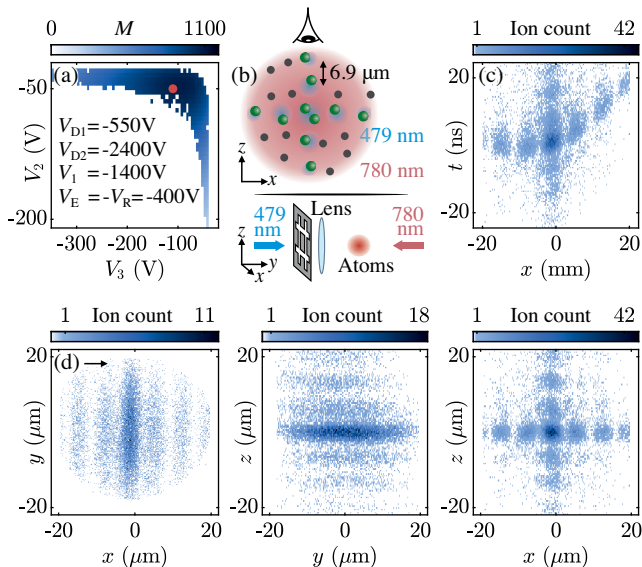
FIG. 7. Three-dimensional imaging. (a) Transverse magnification for a reduced magnitude of V_{D1}, boosting the axial resolution. All electrode voltages are given in the plot. (b) Proof-of-principle experiment to test the 3D imaging. The light field of the 479-nm photoionization laser is spatially structured by projecting the diffraction pattern of two crossed double slits onto the atoms. (c) Imaging result in detector coordinates (xt plane) for an electrode voltage configuration corresponding to the red mark ($V_2 = -50$ V, $V_3 = -110$ V) shown in panel (a). The arrival time of the ions is corrected for an offset. As predicted from simulations, a curvature of the time of flight is observed. (d) Imaging result in object coordinates (all planes) after compensating for the curvature of the time of flight. In both panels (c) and (d), an integration of all ion counts is performed along the dimension not shown.

field was spatially structured in both the x and z directions by projecting the diffraction pattern of two crossed double slits (slit separation and width of 6.5 mm and 1 mm, respectively) onto the atoms [see Fig. 7(b)]. The x period of the cross-shaped diffraction pattern was measured to be 6.9 μm. In order to resolve several diffraction orders in the z direction, the atomic cloud with a $1/e$-diameter of approximately 20 μm was repositioned several times during the measurement.

Figure 7(c) shows the experimental result as a function of the detector coordinates x and t, where, except for an offset, t corresponds to the time of flight of the ions. As expected from Eq. (1), the data exhibit a curvature, the asymmetry of which we attribute to a displacement of the ionization region from the optical axis and to small mechanical asymmetries within the ion optics. In a postprocessing step, we compensate for the temporal distortion by the subtraction of a fitted fourth-order polynomial $p(x, y)$. By assuming equal x and z periods of the diffraction pattern, the distance-to-time conversion factor α can be estimated to be $\alpha \approx 1.12$ ns/μm, which is in

good agreement with our simulations. The postprocessed data are shown in Fig. 7(d) as a function of the object coordinates. The diffraction pattern is clearly resolved in the z direction, corresponding to the optical axis of the microscope.

Because of detrimental effects broadening the arrival time distribution of the ions (see Appendix D), we do not expect the axial resolution to match the transverse resolution in the presented operation mode. As our simulations suggest, axial resolutions significantly better than 1 μm can be achieved, however, for drift-tube voltages V_{D1} even smaller in magnitude. The corresponding operation modes will be investigated in future studies.

IV. CONCLUSION AND OUTLOOK

We have presented a high-resolution ion microscope allowing for the time-resolved probing of quantum gases on a single-atom level. The magnification of the imaging system was shown to be highly tunable, enabling the investigation of both isolated microscopic few-body processes and extended many-body systems. With a resolution better than 200 nm and an exceptionally large DOF of more than 70 μm, our microscope is excellently suited for the study of bosonic and fermionic bulk quantum gases on the length scale of the healing length and the Fermi wavelength, respectively. A pulsed operation mode enables the spatially resolved investigation of ion-atom hybrid systems and Rydberg ensembles and permits the ultraprecise measurement and subsequent compensation of stray electric fields.

We believe that charged-particle optics holds great promise for the field of ultracold quantum gases and will allow for a whole range of new experimental techniques as well as an unprecedented level of precision. Key aspects in this respect are the exceptional spatial and temporal resolution, the possibility of 3D imaging, and the freedom to combine the spatial resolution with spectroscopic techniques. For example, the latter possibility enables spin-resolved detection by employing a Zeeman-sensitive and narrow-line optical transition to a Rydberg state, which is subsequently field ionized.

As a next step, we plan to use the 3D imaging capabilities of our apparatus in combination with near-threshold photoionization to create and study ultracold ionic impurities in a degenerate quantum gas [31,33]. Using the same experimental tools, we also aim for the observation of individual ion-atom collisions in the quantum regime [35].

APPENDIX A: TRAJECTORY SIMULATIONS

The imaging properties of the ion optics were simulated by propagating test patterns through the electrostatic potential corresponding to a given electrode voltage configuration. An example of the axial potential is shown in Fig. 8. As the ions remain well separated under typical experimental conditions, no Coulomb repulsion was considered. For the simulations shown in Figs. 3(a) and 7(a), two test patterns with a lateral line spacing of $L = 100$ nm and an extent of 10 μm along the optical axis were employed [see inset of Fig. 3(a) for the shape of the patterns]. Each pattern consisted of 800 ions, given an isotropic velocity distribution corresponding to an initial kinetic energy of $k_B \times 10$ μK. One of the patterns was centered on the optical axis, whereas the other one was offset by a distance corresponding to 42.5% of the FOV. Here, the FOV is defined as the detector diameter divided by the magnification. For the displayed data points, the line spacing is clearly resolved and the local magnification extracted from the off-axis pattern differs by less than 5% from the on-axis case. The latter condition aims to ensure a low distortion of the imaging result. Since the effects of mechanical asymmetries and voltage noise are not captured by the simulations presented, no quantitative prediction can be made for the resolution.
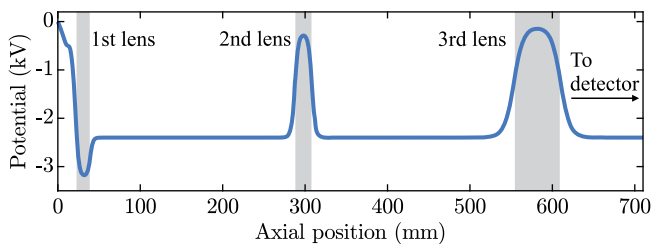
FIG. 8.   Example of the axial electrostatic potential. The curve shown corresponds to an electrode voltage configuration of $[V_R, V_E, V_1, V_2, V_3, V_D] = [500, -500, -3200, -250, -110, -2400]$ V. The shaded regions mark the position of the main electrodes of the three lenses. The potential stays flat for the remaining distance to the detector, which is located at 1350 mm.

APPENDIX B: PREPARATION OF THE ATOMIC CLOUD

Except for the 3D measurement, for which further information can be found in the main text, the following experimental details apply. Each experimental cycle started with the loading of approximately 4×10^8 ^{87}Rb atoms from an effusive oven into a magneto-optical trap (MOT). For this, a double-element Zeeman slower was employed, which in the future will allow us to perform experiments with lithium [47]. The atoms were then optically transported along the x axis (Fig. 2) from the MOT chamber into a separate science chamber, above which the ion microscope is located. The transport was accomplished by the use of a transport trap consisting of two 1064-nm laser beams passing through a lens mounted on an air-bearing translation stage [48]. The beams crossed under a small angle of 2.3°, producing a transverse intensity profile with a $1/e^2$ waist of approximately 70 μm at the crossing point. For the measurements performed at low magnifications [Fig. 3(c)], we typically held 2×10^6 to 3×10^6 atoms at a temperature on the order of 10 μK in the transport trap. For the experiments performed in an optical lattice, we ramped down the power of the transport trap on a timescale of 1.5 s and ramped up the lattice within 100 ms. The latter was produced by a retroreflected 1064-nm laser beam oriented along the y axis (Fig. 2) and possessing a $1/e^2$ waist of $w_{1064} \approx 110$ μm. After the ramping process, the atoms were solely held by the optical lattice potential with a depth of about $1100E_r$, where the recoil energy is defined as $E_r = \hbar^2 k^2 / 2m$. Here, m corresponds to the atomic mass, $\hbar$ is the reduced Planck constant, and k is the wave vector of the lattice light. All experiments were performed in unpolarized samples with the atoms being pumped to the $F = 2$ hyperfine state. Depending on the specific measurement, a complete experimental cycle lasted between 10 and 13 s.

APPENDIX C: PHOTOIONIZATION SEQUENCE

After the preparation of the atomic cloud, a photoionization phase followed. For the measurements performed in the continuous operation mode of the microscope, the ionization sequence lasted 200 ms, during which time the 780-nm laser was switched on continuously. Because of technical reasons, the 479-nm laser was pulsed with a duty cycle of 95% and a frequency of 50 kHz. For the pulsed measurements shown in Fig. 6, the ionization sequence lasted 1.8 s and consisted of 6000 ionization cycles. In each cycle, a 1-μs-long photoionization pulse was followed by a variable wait time t_{wait} (see main text) before the extraction field was pulsed on. In order to minimize the effect of dark counts that occur at a typical rate of a few Hz, the detector was gated such as to register only signals compatible with the employed ionization sequence. The number of detected ions per

experimental cycle (i.e., for one atomic cloud) depends on the specific measurement and typically ranges between a few tens and a few hundreds of ions. As an example, the measurement shown in Fig. 5(a) consists of 18 400 ion counts, which were acquired over the course of one hour.

APPENDIX D: ION DETECTION

The employed delay-line detector offers a spatial and temporal resolution on the order of 100 μm and 200 ps, respectively, and features a maximum continuous detection rate of 1 MHz with a multihit dead time on the order of 10 to 20 ns [41]. For the pulsed operation mode, the time resolution of the ion detection is not limited by the detector but by the temporal jitter of the pulsed extraction and the voltage noise of the lens electrodes, which directly translates into a broadening of the time-of-flight distribution of the ions. From our experimental data, we determine a typical time resolution on the order of a few nanoseconds for drift-tube voltages of $V_{D1} = V_{D2} = -2.4$ kV. The time-of-flight distribution of the measurement shown in Fig. 6(a), for example, possesses a full width at half maximum of approximately 4.5 ns. It is worth noting that the given time resolution applies to the detection of ionic systems and, therefore, does not account for the ionization process itself.

The delay line is combined with two stacked MCPs with an active diameter slightly larger than 40 mm and an open-area ratio (OAR) of 70% (F1217-01 MOD7, Hamamatsu). Since the detection efficiency η of MCPs is typically limited to values close to the OAR [42], we plan to exchange the front MCP with a funnel-type model offering an OAR of 90% [43]. In addition, we envision enhancing the overall quantum efficiency to detect a single ion to higher than 99% using a Rydberg antiblockade effect (see Ref. [44] and references therein), which allows for the resonant laser excitation of Rydberg atoms on a shell around the ion. Because of the Stark effect of Rydberg atoms [39], this shell can have a radius on the order of 1 μm. As the extraction field of the ion microscope is pulsed on, the Rydberg atoms are field ionized, and the initially single ion is converted into n ions (typically $n = 2$–6), such that the infidelity of the detection is reduced to $(1 - \eta)^n$. Since the timescale for the Rydberg excitation can be very fast (around 10 to 100 ns), the proposed scheme can be repeated several times in a single atomic cloud. The secondary ions responsible for the described preamplification process share, on average, a common center of gravity with the initial ion. However, depending on the amplification protocol, a small position noise, as well as a loss of temporal resolution, is introduced. For the specific application, a trade-off between spatial resolution, time resolution, and quantum efficiency needs to be found.

APPENDIX E: DETERMINATION OF THE MAGNIFICATION

For the measurements performed in an optical lattice [see Fig. 3(b)], the FFT corresponding to the integrated lattice profile was fitted assuming a Gaussian shape of the first- and second-order peaks evoked by the periodicity of the lattice. The magnification was then determined from the fitted peak positions and the known wavelength of the lattice laser $\lambda_{lat} = (1063.93 \pm 0.01)$ nm. Error bars were determined by considering the conservative estimate of the systematic error of λ_{lat} and the standard error of the fitted peak positions. For the characterization of small magnifications for which the lattice could not be resolved [see Fig. 3(c)], a spatial structure was induced into the 780-nm photoionization beam by passing the beam through a double slit (slit separation and width of 3 mm and 1 mm, respectively) before focusing the beam onto the atoms. To this end, an in-vacuum aspheric lens with an effective focal length of 26 mm was used. The described setup resulted in an image of the far-field diffraction pattern of the double slit in the focal plane of the lens. The period of the diffraction pattern λ_{diff} was measured at a known magnification previously calibrated with the optical lattice. In comparison with the measurements performed in an optical lattice, the 479-nm beam was enlarged in the x direction to $w_{479x} \approx 100$ μm and the 780-nm beam measured approximately $w_{780x} \approx 2$ μm at the position of the atoms. The magnification was extracted by fitting the imaged diffraction pattern. Error bars were determined by considering the error of λ_{diff} and the standard error of the fitted pattern period. All error bars in Fig. 3 are significantly smaller than the marker size.

APPENDIX F: DATA PROCESSING

The employed detector delivers a time stamp and a position for each detected ion. We compensated for minor distortions of the detector image in the y direction (Fig. 2) by applying a spatially dependent shift to the detected y position of all ions. The spatial distribution of this shift was found by using the regular density modulation of the atomic cloud in the optical lattice as a test pattern (Fig. 4). The local distortion could be interpolated from the discrepancy between the observed lattice phase and the phase expected for an ideal lattice structure [Fig. 4(d)]. We checked that the influence of wave-front aberrations of the lattice beams is small by shifting the image along the x direction of the detector using the electrostatic deflector after the third lens (Fig. 2). At least partly, we attribute the observed distortions to nonlinearities of the detector.

The global phase Φ_g of the detected lattice pattern [see Fig. 4(c) for a specific measurement] is determined by the phase of the retroreflected optical lattice and thus depends on the relative phase between the two counter-propagating lattice beams. Therefore, Φ_g is susceptible to a thermally

caused position drift of the retroreflecting mirror. To compensate for this effect, we sorted the detection events into groups of 100 consecutively detected ions and calculated the FFT corresponding to the integrated lattice profile for each of the groups. We then extracted the global phase of the lattice from the complex amplitude of the first-order FFT peak and corrected for the drift accordingly. Subsequently, the data were binned with a bin size of 100 μm.

For measurements for which the magnitudes of the FFT peaks were extracted, we determined a statistical error of these by considering again groups of 100 consecutively detected ions. For each of the groups, the complex amplitudes of the first- and second-order FFT peaks were determined. An estimate for the error of the peak magnitudes was then found by dividing the standard deviation of the amplitudes by $\sqrt{n_g}$, where n_g is the number of groups.

APPENDIX G: PULSED OPERATION MODE

The measurements shown in Fig. 6 were acquired using the following electrode voltages: $[V_R, V_E, V_1, V_2, V_3, V_D] = [400, -400, -2800, -200, -110, -2400]$ V. For the pulsed measurements shown in Fig. 6(b), the magnitude of the first-order FFT peak decreased with increasing t_{wait}. In order to still accurately compensate for the thermal drift of the lattice, a measurement for $t_{wait} = 0$ μs was performed in every second experiment cycle. The thermal drift of the lattice was then deduced only from these additional measurements and corrected for according to the procedure detailed in the previous paragraph.

APPENDIX H: APPROXIMATION OF THE SINGLE-SITE WAVE FUNCTION

For atoms occupying the lowest energy band of our deep optical lattice, we approximate the single-site wave function by a ground-state harmonic oscillator wave function. To this end, we consider the Taylor expansion of the lattice potential around an energy minimum $V(x) \approx V_0 k^2 x^2$ and find the probability density of the lowest harmonic oscillator state to be

$$|\psi(x)|^2 = \frac{(2mV_0 k^2)^{1/4}}{(\pi\hbar)^{1/2}} \exp\left(-\frac{\sqrt{2mV_0}k}{\hbar} x^2\right). \quad (H1)$$

Here, V_0 is the depth of the lattice potential, m is the atomic mass, and k is the wave vector of the 1064-nm lattice light.

APPENDIX I: COMPENSATION OF STRAY ELECTRIC FIELDS

For the pulsed measurements presented in Fig. 6, stray electric fields within the ionization volume were compensated by applying suitable voltages to the six compensation electrodes. In order to calibrate these voltages on the order of a few tens of millivolts, free ions were observed for up to

70 μs. The compensation voltages were adjusted such as to minimize the displacement of the detected ion distribution as the observation time was increased. For the field component along the optical axis, the time-of-flight information from the ion detection was employed. From the observed spread of the ion cloud, the typical magnitude of residual fields in the transverse direction can be quantified to be on the order of 100 μV/cm over a spherical volume with a diameter of 10 μm.

---

[1] N. N. Das Gupta and S. K. Ghosh, *A Report on the Wilson Cloud Chamber and Its Applications in Physics*, Rev. Mod. Phys. **18**, 225 (1946).

[2] H. Geiger and E. Marsden, *The Laws of Deflexion of α Particles through Large Angles*, Philos. Mag. **25**, 604 (1913).

[3] E. Rutherford, *The Scattering of α and β Particles by Matter and the Structure of the Atom*, Philos. Mag. **21**, 669 (1911).

[4] E. W. Müller and K. Bahadur, *Field Ionization of Gases at a Metal Surface and the Resolution of the Field Ion Microscope*, Phys. Rev. **102**, 624 (1956).

[5] J. C. Bergquist, R. G. Hulet, W. M. Itano, and D. J. Wineland, *Observation of Quantum Jumps in a Single Atom*, Phys. Rev. Lett. **57**, 1699 (1986).

[6] T. Sauter, W. Neuhauser, R. Blatt, and P. E. Toschek, *Observation of Quantum Jumps*, Phys. Rev. Lett. **57**, 1696 (1986).

[7] M. Schellekens, R. Hoppeler, A. Perrin, J. V. Gomes, D. Boiron, A. Aspect, and C. I. Westbrook, *Hanbury Brown Twiss Effect for Ultracold Quantum Gases*, Science **310**, 648 (2005).

[8] T. Jeltes, J. M. McNamara, W. Hogervorst, W. Vassen, V. Krachmalnicoff, M. Schellekens, A. Perrin, H. Chang, D. Boiron, A. Aspect, and C. I. Westbrook, *Comparison of the Hanbury Brown-Twiss Effect for Bosons and Fermions*, Nature (London) **445**, 402 (2007).

[9] T. Gericke, P. Würtz, D. Reitz, T. Langen, and H. Ott, *High-Resolution Scanning Electron Microscopy of an Ultracold Quantum Gas*, Nat. Phys. **4**, 949 (2008).

[10] H. Ott, *Single Atom Detection in Ultracold Quantum Gases: A Review of Current Progress*, Rep. Prog. Phys. **79**, 054401 (2016).

[11] W. S. Bakr, J. I. Gillen, A. Peng, S. Fölling, and M. Greiner, *A Quantum Gas Microscope for Detecting Single Atoms in a Hubbard-Regime Optical Lattice*, Nature (London) **462**, 74 (2009).

[12] C. Gross and I. Bloch, *Quantum Simulations with Ultracold Atoms in Optical Lattices*, Science **357**, 995 (2017).

[13] W. S. Bakr, A. Peng, M. E. Tai, R. Ma, J. Simon, J. I. Gillen, S. Fölling, L. Pollet, and M. Greiner, *Probing the Superfluid–to–Mott Insulator Transition at the Single-Atom Level*, Science **329**, 547 (2010).

[14] J. F. Sherson, C. Weitenberg, M. Endres, M. Cheneau, I. Bloch, and S. Kuhr, *Single-Atom-Resolved Fluorescence Imaging of an Atomic Mott Insulator*, Nature (London) **467**, 68 (2010).

[15] A. Mazurenko, C. S. Chiu, G. Ji, M. F. Parsons, M. Kanász-Nagy, R. Schmidt, F. Grusdt, E. Demler, D. Greif, and M. Greiner, *A Cold-Atom Fermi–Hubbard Antiferromagnet*, Nature (London) **545,** 462 (2017).

[16] M. A. Nichols, L. W. Cheuk, M. Okan, T. R. Hartke, E. Mendez, T. Senthil, E. Khatami, H. Zhang, and M. W. Zwierlein, *Spin Transport in a Mott Insulator of Ultracold Fermions*, Science **363,** 383 (2019).

[17] K. D. Nelson, X. Li, and D. S. Weiss, *Imaging Single Atoms in a Three-Dimensional Array*, Nat. Phys. **3,** 556 (2007).

[18] D. Barredo, V. Lienhard, S. de Léséleuc, T. Lahaye, and A. Browaeys, *Synthetic Three-Dimensional Atomic Structures Assembled Atom by Atom*, Nature (London) **561,** 79 (2018).

[19] M. McDonald, J. Trisnadi, K.-X. Yao, and C. Chin, *Super-resolution Microscopy of Cold Atoms in an Optical Lattice*, Phys. Rev. X **9,** 021001 (2019).

[20] S. Subhankar, Y. Wang, T.-C. Tsui, S. L. Rolston, and J. V. Porto, *Nanoscale Atomic Density Microscopy*, Phys. Rev. X **9,** 021002 (2019).

[21] H. Nguyen, X. Fléchard, R. Brédy, H. A. Camp, and B. D. DePaola, *Recoil Ion Momentum Spectroscopy Using Magneto-Optically Trapped Atoms*, Rev. Sci. Instrum. **75,** 2638 (2004).

[22] B. D. DePaola, R. Morgenstern, and N. Andersen, *MOTRIMS: Magneto–Optical Trap Recoil Ion Momentum Spectroscopy*, Adv. At. Mol. Opt. Phys. **55,** 139 (2008).

[23] M. Stecker, H. Schefzyk, J. Fortágh, and A. Günther, *A High Resolution Ion Microscope for Cold Atoms*, New J. Phys. **19,** 043020 (2017).

[24] R. M. W. van Bijnen, C. Ravensbergen, D. J. Bakker, G. J. Dijk, S. J. J. M. F. Kokkelmans, and E. J. D. Vredenbregt, *Patterned Rydberg Excitation and Ionization with a Spatial Light Modulator*, New J. Phys. **17,** 023045 (2015).

[25] A. Schwarzkopf, R. E. Sapiro, and G. Raithel, *Imaging Spatial Correlations of Rydberg Excitations in Cold Atom Clouds*, Phys. Rev. Lett. **107,** 103001 (2011).

[26] A. Schwarzkopf, D. A. Anderson, N. Thaicharoen, and G. Raithel, *Spatial Correlations between Rydberg Atoms in an Optical Dipole Trap*, Phys. Rev. A **88,** 061406(R) (2013).

[27] D. P. Fahey, T. J. Carroll, and M. W. Noel, *Imaging the Dipole-Dipole Energy Exchange between Ultracold Rubidium Rydberg Atoms*, Phys. Rev. A **91,** 062702 (2015).

[28] M. Stecker, R. Nold, L.-M. Steinert, J. Grimmel, D. Petrosyan, J. Fortágh, and A. Günther, *Controlling the Dipole Blockade and Ionization Rate of Rydberg Atoms in Strong Electric Fields*, Phys. Rev. Lett. **125,** 103602 (2020).

[29] T. Schmid, *Rydberg Molecules for Ultracold Ion-Atom Scattering*, Ph.D. thesis, Universität Stuttgart, 2019.

[30] F. Engel, T. Dieterle, T. Schmid, C. Tomschitz, C. Veit, N. Zuber, R. Löw, T. Pfau, and F. Meinert, *Observation of Rydberg Blockade Induced by a Single Ion*, Phys. Rev. Lett. **121,** 193401 (2018).

[31] M. Tomza, K. Jachymski, R. Gerritsma, A. Negretti, T. Calarco, Z. Idziaszek, and P. S. Julienne, *Cold Hybrid Ion-Atom Systems*, Rev. Mod. Phys. **91,** 035001 (2019).

[32] T. Dieterle, M. Berngruber, C. Hölzl, R. Löw, K. Jachymski, T. Pfau, and F. Meinert, *Transport of a Single Cold Ion Immersed in a Bose-Einstein Condensate*, Phys. Rev. Lett. **126,** 033401 (2021).

[33] G. E. Astrakharchik, L. A. Peña Ardila, R. Schmidt, K. Jachymski, and A. Negretti, *Ionic Polaron in a Bose-Einstein Condensate*, arXiv:2005.12033.

[34] T. Feldker, H. Fürst, H. Hirzler, N. V. Ewald, M. Mazzanti, D. Wiater, M. Tomza, and R. Gerritsma, *Buffer Gas Cooling of a Trapped Ion to the Quantum Regime*, Nat. Phys. **16,** 413 (2020).

[35] T. Schmid, C. Veit, N. Zuber, R. Löw, T. Pfau, M. Tarana, and M. Tomza, *Rydberg Molecules for Ion-Atom Scattering in the Ultracold Regime*, Phys. Rev. Lett. **120,** 153401 (2018).

[36] P. Schauß, M. Cheneau, M. Endres, T. Fukuhara, S. Hild, A. Omran, T. Pohl, C. Gross, S. Kuhr, and I. Bloch, *Observation of Spatially Ordered Structures in a Two-Dimensional Rydberg Gas*, Nature (London) **491,** 87 (2012).

[37] K. Riechers, K. Hueck, N. Luick, T. Lompe, and H. Moritz, *Detecting Friedel Oscillations in Ultracold Fermi Gases*, Eur. Phys. J. D **71,** 232 (2017).

[38] M. Szilagyi, *Electron and Ion Optics* (Plenum Press, New York, 1988).

[39] R. Löw, H. Weimer, J. Nipper, J. B. Balewski, B. Butscher, H. P. Büchler, and T. Pfau, *An Experimental and Theoretical Guide to Strongly Interacting Rydberg Gases*, J. Phys. B **45,** 113001 (2012).

[40] O. Jagutzki, V. Mergel, K. Ullmann-Pfleger, L. Spielberger, U. Spillmann, R. Dörner, and H. Schmidt-Böcking, *A Broad-Application Microchannel-Plate Detector System for Advanced Particle or Photon Detection Tasks: Large Area Imaging, Precise Multi-hit Timing Information and High Detection Rate*, Nucl. Instrum. Methods Phys. Res. **477,** 244 (2002).

[41] DLD40EP, RoentDek.

[42] J. Oberheide, P. Wilhelms, and M. Zimmer, *New Results on the Absolute Ion Detection Efficiencies of a Microchannel Plate*, Meas. Sci. Technol. **8,** 351 (1997).

[43] K. Fehre, D. Trojanowskaja, J. Gatzke, M. Kunitski, F. Trinter, S. Zeller, L. P. H. Schmidt, J. Stohner, R. Berger, A. Czasch, O. Jagutzki, T. Jahnke, R. Dörner, and M. S. Schöffler, *Absolute Ion Detection Efficiencies of Micro-channel Plates and Funnel Microchannel Plates for Multi-coincidence Detection*, Rev. Sci. Instrum. **89,** 045112 (2018).

[44] A. Urvoy, F. Ripka, I. Lesanovsky, D. Booth, J. P. Shaffer, T. Pfau, and R. Löw, *Strongly Correlated Growth of Rydberg Aggregates in a Vapor Cell*, Phys. Rev. Lett. **114,** 203002 (2015).

[45] SIMION 8.1.1.32, Scientific Instrument Services.

[46] J. R. Abo-Shaeer, C. Raman, J. M. Vogels, and W. Ketterle, *Observation of Vortex Lattices in Bose-Einstein Condensates*, Science **292,** 476 (2001).

[47] G. E. Marti, R. Olf, E. Vogt, A. Öttl, and D. M. Stamper-Kurn, *Two-Element Zeeman Slower for Rubidium and Lithium*, Phys. Rev. A **81,** 043424 (2010).

[48] C. Gross, H. C. J. Gan, and K. Dieckmann, *All-Optical Production and Transport of a Large ^{6}Li Quantum Gas in a Crossed Optical Dipole Trap*, Phys. Rev. A **93,** 053424 (2016).